

Short communication

3D rotational shear wave elasticity imaging (3D-RSWEI) in anisotropic lattice phantoms

Shruthi Srinivasan ^a*, Kevin N. Eckstein ^b, Daniel Yoon ^b, Ned C. Rouze ^a, Kaden D. Bock ^a, Estela Villacis ^b, Philip V. Bayly ^b, Kathryn R. Nightingale ^a

^a Department of Biomedical Engineering, Duke University, Durham, NC, United States

^b Mechanical Engineering and Materials Science, Washington University, St. Louis, MO, United States

ARTICLE INFO

Keywords:

Calibrating phantoms
Shear wave elasticity imaging
Anisotropy
Lattice structure
Mechanical testing

ABSTRACT

We present ultrasonic 3D rotational shear wave elasticity imaging (3D-RSWEI) characterization of anisotropic 3D-printed hydrogel lattice phantoms that were originally developed for magnetic resonance elastography (MRE) applications. Shear wave speeds versus rotational angle were measured for two 3D-printed hydrogel lattices while submerged in water and after embedding in different stiffnesses of isotropic poly-vinyl alcohol (PVA). Shear wave propagation in the lattices was anisotropic, with faster wave speeds parallel to the scaling direction of the lattices. We observed that shear wave speeds and shear anisotropy decreased when the lattices were embedded in PVA versus submerged in water. Shear wave dispersion was observed in the lattice+PVA phantoms, with greater dispersion in the direction parallel to the scaling direction versus perpendicular. Dynamic shear testing results of the lattice+PVA phantoms were compared to 3D-RSWEI characterization with differences of 8.4% and 24.1% for propagation parallel and perpendicular to the scaling direction. These results demonstrate the feasibility of ultrasonic SWEI characterization of novel anisotropic MRE lattice phantoms.

1. Introduction

Shear wave elasticity imaging (SWEI) is a non-invasive technique which uses ultrasound to characterize the stiffness of biological tissues. Shear waves are generated by an acoustic radiation force excitation, after which their propagation is tracked using traditional ultrasonic methods. Estimated shear wave speeds SWS and assumed density ρ can then be used to estimate the shear modulus μ of the material under assumptions of linear elasticity and incompressibility through the expression

$$\mu = \rho(SWS)^2. \quad (1)$$

This expression is not valid in anisotropic materials, which have varying mechanical properties in different directions. Many biological tissue types exhibit anisotropy, like skeletal muscle (Morrow et al., 2010; Knight et al., 2022), brain tissue (Prange and Margulies, 2002; Smith et al., 2022; Feng et al., 2013), and myocardial tissue (Dwyer and Coulombe, 2021; Emig et al., 2021; Urban et al., 2016). Previous work has shown the promise of 3D Rotational SWEI (3D-RSWEI) to fully characterize anisotropic materials such as skeletal muscle by collecting multiple SWEI measurements at different transducer rotational angles (Knight et al., 2022; Paley et al., 2023). Skeletal muscle is

often characterized as a transversely isotropic material, with a material symmetry axis in the direction of the muscle fibers (Morrow et al., 2010). In homogeneous, linear elastic, and incompressible transversely isotropic materials with the acoustic radiation force applied normal to the material symmetry axis, the estimated group shear wave speeds versus rotational angle are elliptical (Rouze et al., 2020):

$$\rho(SWS(\phi_{rot}))^2 = \frac{\mu_T \mu_L}{(\mu_T \cos^2(\phi_{rot}) + \mu_L \sin^2(\phi_{rot}))}. \quad (2)$$

In Eq. (2), ϕ_{rot} is the rotational angle with respect to the material symmetry axis, and μ_L and μ_T are the shear moduli parallel and perpendicular to this axis respectively. Therefore, fitting an elliptical shape using 3D-RSWEI allows for the estimation of μ_L and μ_T , which can also be used to characterize shear anisotropy (χ_μ) (Tweten et al., 2015):

$$\chi_\mu = \frac{\mu_L - \mu_T}{\mu_T}. \quad (3)$$

There exists an unmet need for reproducible anisotropic tissue-mimicking elastic phantoms to calibrate and cross-validate elastography techniques, such as 3D-RSWEI and magnetic resonance elastography (MRE). There is a breadth of existing work attempting to address

* Corresponding author.

E-mail address: shruthi.srinivasan@duke.edu (S. Srinivasan).

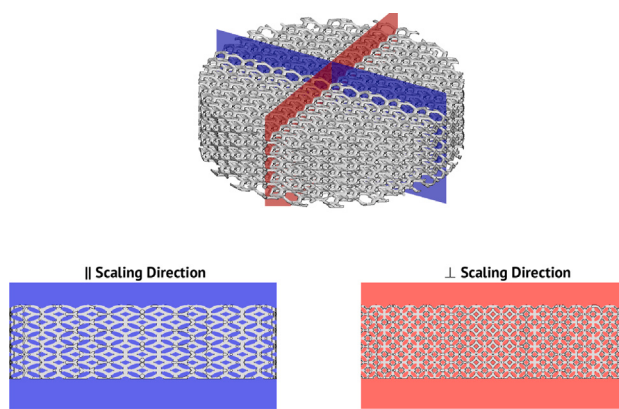


Fig. 1. Design of anisotropic lattice with scaled unit cells with dimensions of $2 \times 2 \times 4$ mm 3 .

this need. Phantom fabrication protocols to mimic the mechanical properties of isotropic tissues have used gelatin and agar gel (Morrow et al., 2010; Pietsch et al., 2014; Gennisson et al., 2010), polyvinyl alcohol (PVA) cryogel (Surry et al., 2004; Dong and Lee, 2022; Fromageau et al., 2003), and polyacrylamide (PAA) gel (Usumura et al., 2021; Kumar et al., 2010). Existing methods for introducing anisotropy in non-biological materials involve an applied uniaxial (Caenen et al., 2020; Chatelin et al., 2014) or torsional (Fiorentini et al., 2023) strain to isotropic PVA. Other methods involve embedding fibers in a soft homogeneous background material, using materials such as nylon monofilaments (Aristizabal et al., 2014), polyester materials (Aristizabal et al., 2014), or stiffer gelatin (Guidetti et al., 2019) for the fiber structure. However, these methods face challenges with repeatability, and often involve custom equipment for fabrication. Bovine and porcine *ex vivo* phantoms are also used in SWEI and MRE studies to capture the anisotropy of *in vivo* biological tissue (Wang et al., 2013; Zhou et al., 2020). However, *ex vivo* models are not longitudinally viable as mechanical properties change post-mortem, and the tissue will suffer from decay over time (Wang et al., 2024; Wei et al., 2022). Additionally, it is difficult to achieve consistent mechanical properties between *ex vivo* samples, therefore they cannot be used reproducibly for calibration purposes.

Anisotropic phantom fabrication for magnetic resonance elastography has recently exploited 3D-printing techniques such as ink-jet or extrusion printing, and digital light processing (DLP). Structural repeatability of 3D printed materials allows for increased scalability. These processes use bio-inks or bio-resins to closely match the material densities and stiffness of biological tissue for a variety of applications (Paulsen et al., 2021; Wei et al., 2022).

Herein we present a 3D-RSWEI characterization of 3D-printed scaled lattice hydrogel phantoms. Designed and fabricated by methods described in Yoon et al. (2023), these lattices have been characterized using dynamic shear testing methods and gelatin-embedded lattices successfully demonstrated anisotropy in a magnetic resonance elastography study (Yoon et al., 2024; Eckstein et al., 2024). We embedded these lattices in a PVA background material and characterized the mechanical and acoustic properties of these composite phantoms using 3D-RSWEI (Knight et al., 2022) and standard acoustic property measurement methods (American Institute of Ultrasound in Medicine, 2014). Additionally, we compared our SWEI characterization to dynamic shear testing measurements.

2. Methods

2.1. Lattice structure

Design and printing techniques are described in Yoon et al. (2023). Briefly, lattice geometries were generated with computer aided design

Table 1

Recipes used for fabrication of PVA materials, expressed in mass wt. percentage. Coolant was pure ethylene glycol.

	PVA	Coolant	DI water	Cellulose
Phantom #1	8	36.4	54.6	1
Phantom #2	4	38.0	57.0	1

software (Grasshopper3D and Rhinoceros® 3D v7.0, Robert McNeel & Associates; IntraLattice plugin, ADM, McGill University) and printed from polyethylene glycol di-acrylate (PEGDA Start, CELLINK) using digital light processing (Lumen X+, CELLINK). Each lattice was comprised of vintile unit cells geometrically scaled in one direction to create anisotropic structures. A rendering of the lattice design is shown in Fig. 1. Unit cells measured $2 \times 2 \times 4$ mm 3 with a 300 μm strut diameter. Larger lattice disks were printed for SWEI characterization (8.8 mm height, 35 mm dia.) and smaller samples for dynamic shear testing measurements (4 mm height, 15 mm dia.).

2.2. Polyvinyl Alcohol (PVA) and embedding lattice

PVA at two different concentrations were used as the homogeneous background material (see Table 1), following the preparation reported in Surry et al. (2004).

Both recipes are expressed in terms of mass weight, containing PVA (PVA 98%–99% hydrolyzed, Alfa Aesar, Ward Hill, MA), ethylene glycol coolant (Concentrate Antifreeze, Prestone, Chicago, IL, USA), deionized water, and cellulose (20 20 μm , Sigma Life Science, Darmstadt, Germany) to introduce acoustic scattering properties.

The lattices were embedded in the un-crosslinked PVA solution at a temperature of 25 °C, within the temperature sensitivity of the PEGDA Start (temperature must be below 30 °C to prevent lattice shrinkage and temperature sensitive degradation). Samples of homogeneous PVA were made from this fabrication batch as well, for comparison. Both phantoms underwent one 12-h freezing cycle at -20 °C, then a 12-h thawing cycle.

2.3. 3D-RSWEI acquisition

Data were acquired using a Verasonics research ultrasound scanner (Verasonics Vantage 256®, Kirkland, VA) and an L11-5V probe. For each planar SWEI acquisition, we generated an acoustic radiation force excitation (6 MHz, 400 cycles, F/1 aperture, 18 mm focal depth) to generate a propagating shear wave. The shear wave was then tracked for 25 ms imaging with a center frequency of 8 MHz, with 3 plane waves steered at -3°, 0°, and 3° at a pulse repetition frequency of 14.3 kHz. This planar SWEI acquisition was repeated while continuously rotating the transducer about its central axis for a 180° rotation, collecting data in 5° increments. The rotation of the transducer was accomplished using a robotic arm (Universal Robots UR10e, CIMTEC Automation, NC) at a speed of 40°/s. Each repeat acquisition was conducted by repositioning the robot over the lattice for different speckle realizations. Once each lattice sample was embedded in PVA, measurements were conducted while the phantoms were submerged in an antifreeze mixture (40% ethylene glycol and 60% water) to prevent leaching of this solution from the phantom over time (Bisht et al., 2024). All data collection was performed at room temperature and on an optical table, as shown in Fig. 2.

2.4. SWEI data processing and dispersion analysis

Axial particle velocity was estimated using the algorithm described by Kasai et al. (1985), which was applied to beamformed IQ data using a 6λ kernel size. Before estimating shear wave speed, we applied temporal bandpass filters to particle velocity data with cutoff frequencies at 50 and 1000 Hz, a spatial high pass filter with a cutoff frequency

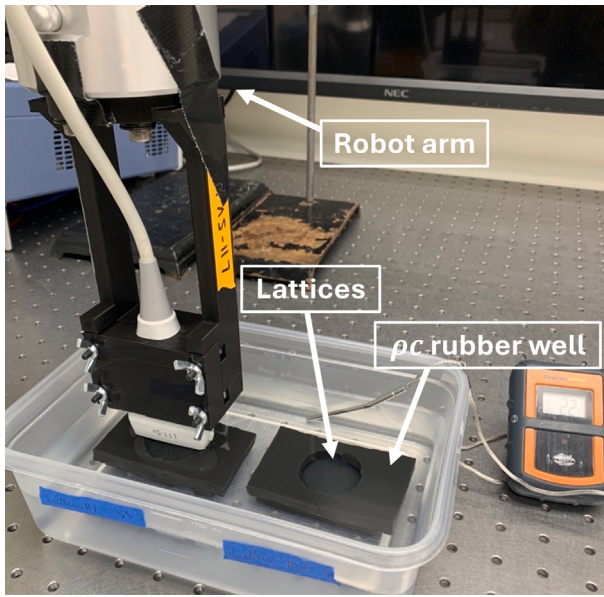


Fig. 2. Setup of rotational 3D-RSWEI acquisition, robot arm was used to position the probe and rotate transducer about the central axis. The lattices were held in place by pc-rubber “wells” to prevent movement during data collection.

at 50 cycles/mm, and radial amplitude compensation to account for geometric spreading of the wave (Paley et al., 2023). Shear wave speeds were estimated at discrete axial depths for each rotational angle using a radon-sum approach (Rouze et al., 2010), averaging shear wave motion 0.5 mm above and below the depth-of-interest. Shear wave speeds as a function of rotational angle were fit to Eq. (2) using a Random Sample Consensus (RANSAC) method (Paley et al., 2024). Shear wave speeds parallel and perpendicular to the scaling direction were then estimated from the major and minor axis respectively of the fitted ellipse. Acquisitions were excluded from processing if the elliptical fit did not meet quality thresholds (fitted RMSE < 0.22 Paley et al., 2023).

Dispersion curves for each lattice sample were estimated at each rotational angle by taking the 2D Fast Fourier transform (2DFFT) of the space-time planes constructed at the focal depth (Alleyne and Cawley, 1991). Phase velocity v vs. temporal frequency f curves were calculated by dividing each temporal frequency in the 2D-FFT by the corresponding peak spatial frequency,

$$v(f) = \frac{f}{k_{f,max}} \quad (4)$$

Following Rouze et al. (2018), dispersion curves were parameterized based on linear slope fitting at a reference frequency. Reference frequencies were chosen based on the center of the shear wave bandwidth in each phantom (400 Hz for lattice # 1 in 8% PVA, and 150 Hz for lattice # 2 in 4% PVA).

2.5. Acoustical characterization

We measured speed-of-sound and acoustic attenuation in the lattice+PVA phantoms using through-transmission techniques (American Institute of Ultrasound in Medicine, 2014). We used linear array transducers on a Verasonics Vantage scanner to transmit a diverging-wave and received the pulse using a membrane hydrophone (HMA-0200, Onda Corporation, Sunnyvale, CA) in a pitch-catch configuration. A Philips ATL L7-4 transducer was used for the speed-of-sound measurements, and both an L7-4 and a Verasonics L11-5V transducer were used to measure acoustic attenuation within the frequency range of 4–10 MHz. Speckle SNR was calculated by dividing the mean by the standard deviation of the envelope detected B-mode pixel brightness, in a region-of-interest defined within the phantom (shown, for example, in Fig. 4, dashed lines) (Dutt and Greenleaf, 1995).

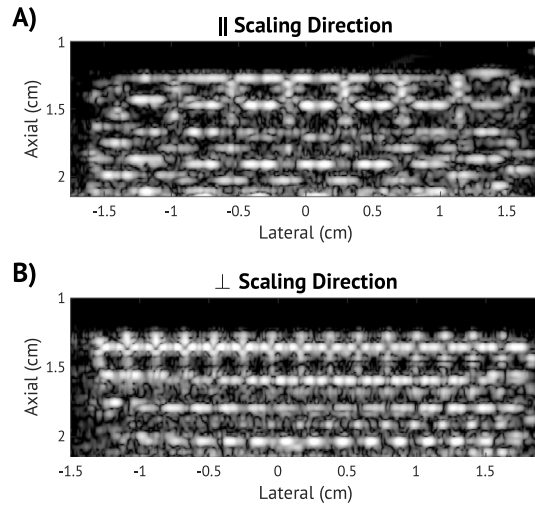


Fig. 3. B-mode images of lattice #1 submerged in water. Cross sectional views parallel (A) and perpendicular (B) to the scaling direction.

Table 2

SWS estimates (mean \pm standard deviation) from 8 repeated acquisitions in both lattice samples submerged in water.

	$SWS_{ }$ (m/s)	SWS_{\perp} (m/s)	χ_{μ}
Lattice #1	7.69 ± 0.24	4.18 ± 0.20	2.44 ± 0.48
Lattice #2	6.63 ± 0.46	2.93 ± 0.24	4.23 ± 0.82

2.6. Dynamic shear testing

Measurements of complex shear moduli in directions parallel and perpendicular to the lattice scaling direction were obtained by dynamic shear testing (DST) of disk-shaped (15 mm dia., ~3 mm thick) lattice samples. Methods of DST have been previously described (Feng et al., 2013; Yoon et al., 2023; Okamoto et al., 2011). Horizontal (shear) displacement of ~100 μ m was applied to the top surface of samples, driven by a “chirp” sweeping across 0–100 Hz frequencies using a voice-coil actuator (LA15-16-024A, BEI Kimco). An 8% compressive strain was applied prior to testing to ensure contact and minimize slipping (Chen et al., 2005). Force and displacement were recorded across a frequency range of 20–100 Hz to estimate complex-valued shear moduli.

2.7. Statistical analysis

We compared shear wave speeds parallel and perpendicular to the scaling direction, within and between phantom samples using Student's t-tests, following Shapiro-Wilk testing for normality. Both tests used a significance level of $\alpha = 0.05$.

3. Results

3.1. Lattice in water measurements

The scaled vintile structure of the unit cells was visible during B-Mode imaging while the lattice was submerged in water (Fig. 3). Shear wave speeds parallel and perpendicular to the scaling direction and shear anisotropy χ_{μ} were averaged across eight repeat rotational acquisitions and are reported in Table 2. Measurements collected using 3D-RSWEI followed a normal distribution between 8 repeat acquisitions. These data demonstrated significant differences in shear wave speeds parallel versus perpendicular to the scaling direction within each lattice ($p < 0.05$). There were also significant differences between shear wave speeds in the same directions between lattices ($p < 0.05$).

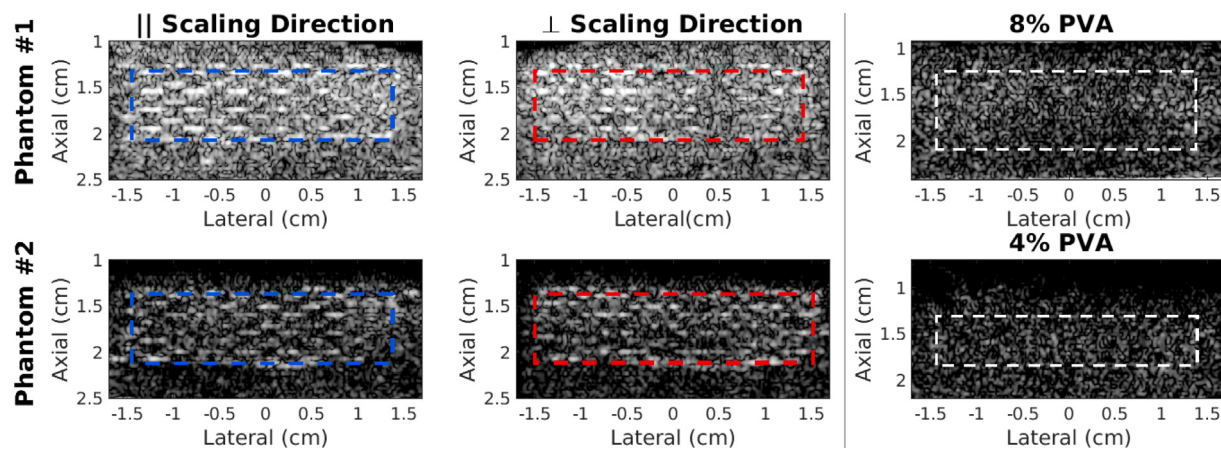


Fig. 4. B-mode images of both composite phantoms and homogeneous PVA samples. Bounds of the embedded lattice are outlined in dashed blue and red lines for cross-sections parallel and perpendicular to the scaling direction respectively. B-mode images of homogeneous PVA are shown in rightmost column. All speckle SNR calculations were made within the dashed region-of-interest.

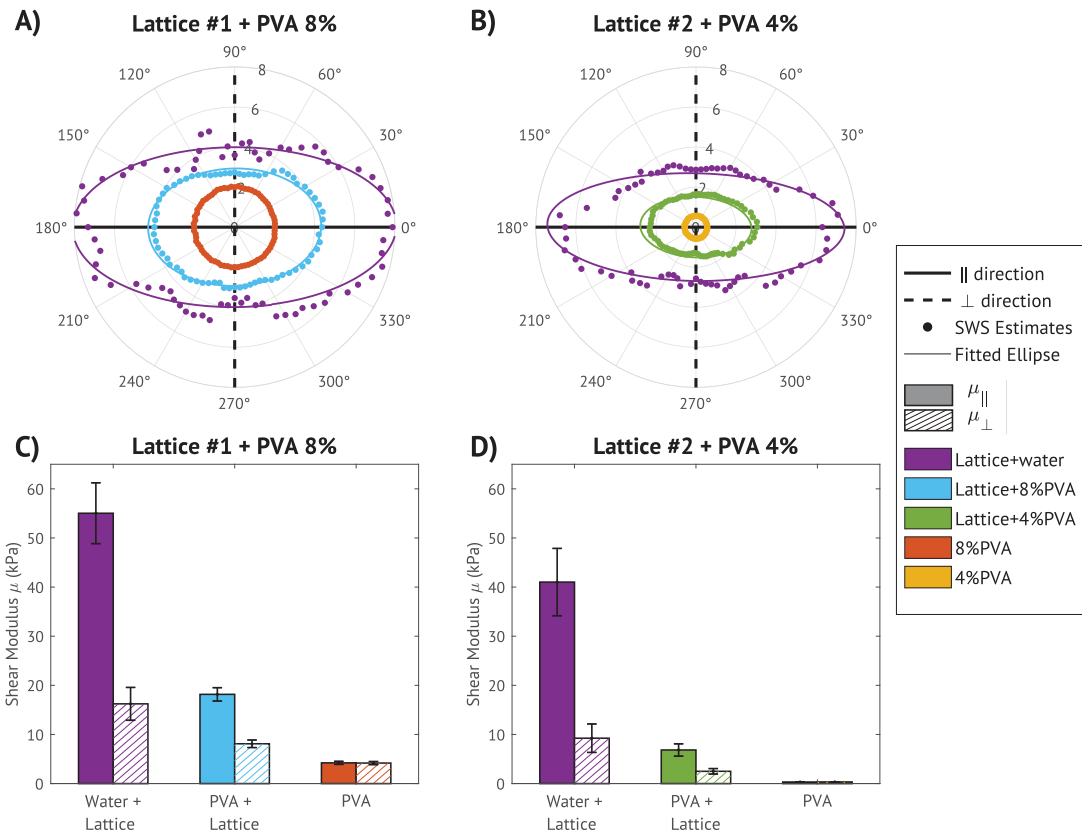


Fig. 5. A, B: Sample shear wave speed estimates (dots) and fitted ellipses (solid line) vs. rotational angle in (A) lattice #1 embedded in 8% PVA and (B) lattice #2 embedded in 4% PVA. Speed estimates are reported in units of m/s. Measurements are provided for lattice+water, lattice+PVA, and corresponding homogeneous PVA samples for each phantom. Parallel (solid black axis) and perpendicular (dashed black axis) to the scaling direction are also denoted. C, D: Estimates of shear moduli parallel and perpendicular to the scaling direction.

Table 3

SWS, shear anisotropy χ_μ , speed of sound c , acoustic attenuation α , and speckle SNR in the embedded lattice+PVA phantoms and corresponding homogeneous PVA samples. Data is reported as mean \pm standard deviation from 8 repeated measurements.

	SWS (m/s)	SWS _⊥ (m/s)	χ_μ	c (m/s)	α (dB/cm/MHz)	Speckle SNR (mean/std)
Phantom #1	4.29 ± 0.08	2.89 ± 0.07	1.20 ± 0.13	1649.65 ± 18.53	0.72 ± 0.12	1.44 ± 0.07
Phantom #2	2.65 ± 0.15	1.59 ± 0.08	1.90 ± 0.39	1629.15 ± 14.43	0.66 ± 0.12	1.23 ± 0.07
8% PVA	2.06 ± 0.08		0.03 ± 0.01	1645.03 ± 3.95	0.86 ± 0.08	1.78 ± 0.04
4% PVA	0.57 ± 0.00		0.04 ± 0.01	1653.43 ± 14.54^a	1.10 ± 0.05^a	1.80 ± 0.04^a

^a Acoustic attenuation and speckle SNR calculations reported in pure 4% PVA even though considerable scatterer settling was observed (seen in Fig. 4).

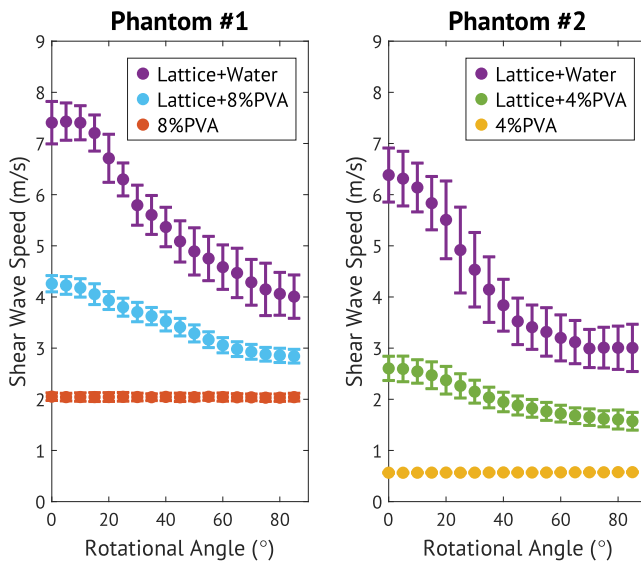


Fig. 6. SWS versus angle in lattice+water, lattice+PVA, and pure PVA in phantom #1 and #2. Error bars represent standard deviation of 8 repeated acquisitions. 0° and 90° correspond to parallel and perpendicular to the scaling direction.

3.2. SW propagation in embedded Lattice+PVA

Lattices were embedded in PVA backgrounds of different stiffnesses ($\mu_{8\%PVA} = 4.20 \pm 0.34$ kPa, $\mu_{4\%PVA} = 0.34 \pm 0.00$ kPa). Herein we refer to lattice #1 embedded in 8% PVA as Phantom #1, and lattice #2 embedded in 4% PVA as Phantom #2.

Fig. 4 shows B-mode images of both lattice phantoms, when the transducer is oriented parallel and perpendicular to the scaling direction. Embedding the lattice in PVA reduced its visibility in the B-mode images, due to the introduction of acoustic scatterers in the PVA. Homogeneous 4% PVA B-mode images (Fig. 4 bottom) show an inhomogeneous speckle pattern due to acoustic scatterer settling. Fig. 5 shows shear wave speeds and shear moduli estimates for both phantoms. Shear moduli parallel and perpendicular to the scaling direction were significantly different for 3D-RSWEI measurements in lattices (Fig. 5C, D). Shear moduli estimates were also significantly different between homogeneous PVA and the respective lattice-embedded PVA phantoms.

Fig. 6 shows shear wave speeds versus rotational angle for both phantoms through multiple acquisitions. Once the lattices were transferred from a water background to PVA background, measured SWS decreased at all rotational angles. In Phantom #1, SWS decreased by $42.3 \pm 3.9\%$ parallel and $28.3 \pm 8.6\%$ perpendicular to the scaling direction. In Phantom #2, shear wave speeds decreased $58.9 \pm 5.1\%$ parallel and $46.5 \pm 10.3\%$ perpendicular to the scaling direction. Shear anisotropy (Eq. (3)) decreased by 50% in phantom #1 and by 58% in phantom #2 after embedding.

3.3. Dispersion analysis

Fig. 7 shows averaged dispersion curves for phantom #1 and #2. Dispersion curve data from phantom #2 were noisy at higher frequencies and were discarded beyond 250 Hz. In both phantoms, dispersion slope estimates were higher parallel vs. perpendicular to the scaling direction. Fig. 8 quantifies dispersion slope as a function of rotational angle. Average dispersion slope estimates for phantom #1 were 3.67 ± 0.57 m/s/kHz parallel, and 1.14 ± 0.89 m/s/kHz perpendicular to the scaling direction, in phantom #2 these were 7.09 ± 0.70 m/s/kHz and 3.42 ± 0.75 m/s/kHz, respectively. Dispersion slopes

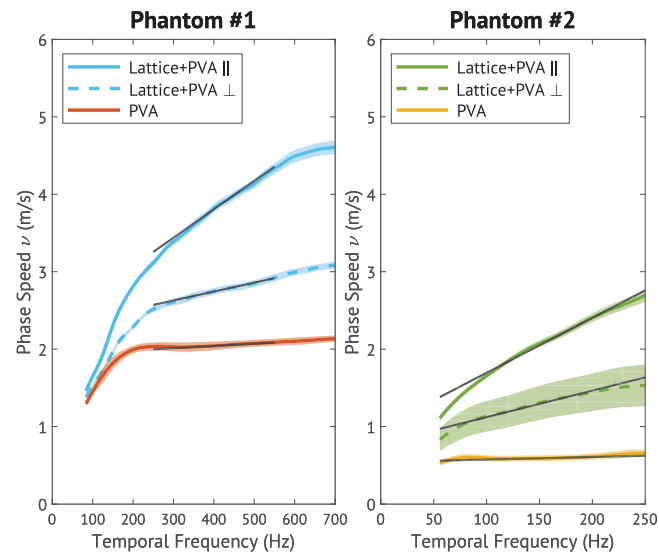


Fig. 7. Phase speed versus frequency in phantom #1 and #2. Dispersion curves for shear wave propagation parallel and perpendicular to the scaling direction, and in homogeneous PVA. Each curve is the average of 8 repeat acquisitions, with 95% confidence intervals plotted using shading of the same color. Linear dispersion slope estimates (shown using black line) taken at a reference frequency of 400 Hz for phantom #1 and 150 Hz for phantom #2. Note that the horizontal axes for two different phantoms show different frequency ranges.

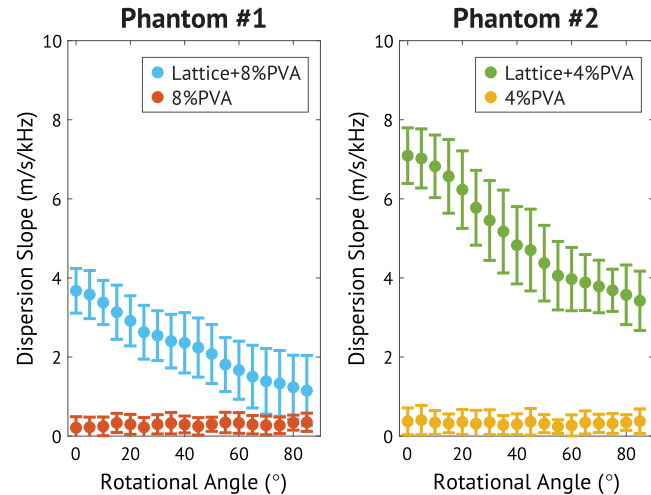


Fig. 8. Dispersion slope estimates as a function of rotational angle in (a) Phantom #1 (at 400 Hz) and (b) Phantom #2 (150 Hz). Error bars represent standard deviation from 8 repeat acquisitions. 0° and 90° correspond to parallel and perpendicular to the scaling direction.

were 0.28 ± 0.24 m/s/kHz in pure 8% PVA and 0.33 ± 0.27 m/s/kHz in 4% PVA.

3.4. Acoustic characterization

Table 3 shows the measured speed-of-sound and acoustic attenuation for each phantom. Speed-of-sound was not significantly different between the lattice-embedded phantoms and the corresponding homogeneous PVA samples. Acoustic attenuation demonstrated a decreasing trend when the lattices were embedded, although this decrease was only significant for phantom #2 ($p < 0.05$). Speckle SNR also decreased when the lattices were embedded: it was 29.4% lower between 8% PVA and phantom #1, and 15.2% lower between pure 4% PVA and phantom #2.

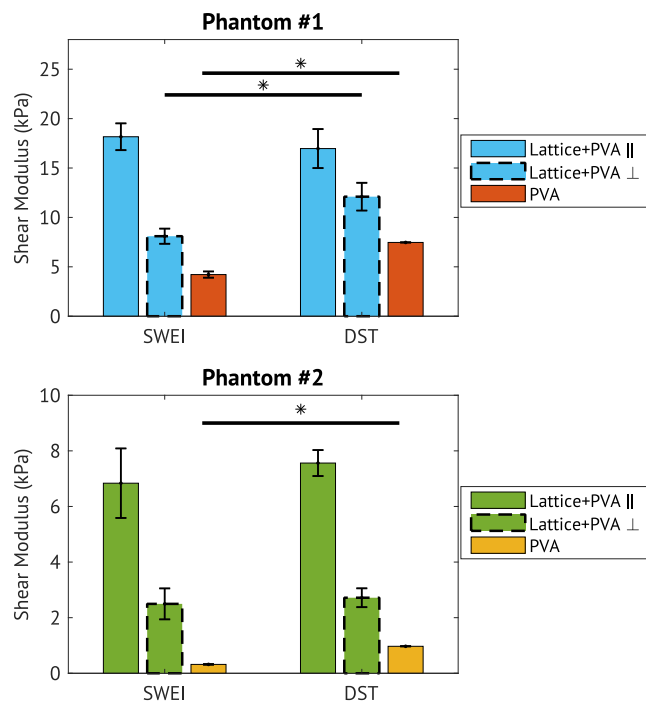


Fig. 9. Shear moduli (kPa) estimates obtained with SWEI and real shear modulus from DST measurement methods, for both phantoms. (*) indicates statistically significant differences ($p < 0.05$ for a 2-way t-test).

3.5. Dynamic shear testing results

Fig. 9 compares shear modulus estimates from SWEI (from Fig. 5C, D) and DST methods. Measured real shear modulus (G') was approximately 10x imaginary shear modulus (G'') for all samples by DST methods; therefore, the real shear modulus was reported as “DST shear modulus”. In Phantom #1, shear modulus estimates from DST measurements were 16.97 ± 1.97 kPa parallel, and 12.10 ± 1.40 kPa perpendicular to the scaling direction, while shear modulus estimates in Phantom #2 were 7.56 ± 0.47 kPa and 2.72 ± 0.34 kPa in the same directions. Shear moduli estimates from DST were 7.51 ± 0.96 kPa in 8% PVA, and 0.96 ± 0.12 kPa in 4% PVA. SWEI and DST measurements agreed in Phantom #2. In Phantom #1 perpendicular to the scaling direction, SWEI and DST measurements were 39.6% different. SWEI and DST measurements in 8% and 4% PVA samples were also significantly different (55.7% and 101.0% different, respectively).

4. Discussion

4.1. SW behavior with changing background material

For both lattice samples submerged in water, shear wave speeds were significantly higher parallel versus perpendicular to the scaling direction, demonstrating expected anisotropic behavior. We observed that shear wave speeds measured in the composite lattice+PVA were between values measured in the lattice+water case and isotropic PVA at every rotational angle (Fig. 6). This was the case for both phantom samples. These results match our expectations for fiber-reinforced composite materials, in which the stiffness of a soft, isotropic and homogeneous material will increase when stiffer fibers or structures are embedded (Arao et al., 2015). When embedded in PVA, both phantoms had higher shear moduli estimates than values observed in *in vivo* muscle (Paley et al., 2023; Dorado Cortez et al., 2016) though shear anisotropy estimates were similar to values estimated in passively stretched muscle at various joint flexion states (Paley et al., 2024).

4.2. Wave dispersion in lattice+PVA phantom

The presence of dispersion (frequency dependent shear wave speed) can be attributed to viscosity and/or to structured wave-guidance. We observed significant shear wave dispersion in both composite lattice phantoms, with greater dispersion parallel vs. perpendicular to the direction of scaling (Fig. 8, $p < 0.05$). In contrast, we observed minimal dispersion in homogeneous 8% and 4% PVA, indicating primarily elastic behavior. We thus posit that the observed wave dispersion in the composite lattices can be primarily attributed to boundary interactions and waveguiding in the lattice structure.

4.3. DST vs. SWEI characterization

We observed reasonable agreement between DST and 3D-RSWEI measurements of shear modulus (Fig. 9, on average 23.3% different in Phantom #1 and 9.31% different in Phantom #2). We hypothesize differences between DST and 3D-RSWEI results can be attributed to varying measurement frequency ranges between DST and 3D-RSWEI characterizations: shear wave bandwidth was 80–700 Hz in Phantom #1 and 50–250 Hz in Phantom #2, DST measurement frequencies were between 20–100 Hz. Frequency-dependent viscoelastic behavior may result in different stiffness measures when differing frequency ranges are used (Okamoto et al., 2011; Oudry et al., 2009). Additionally, slight compression applied during dynamic shear testing (8%) can increase the shear modulus of the PVA or composite phantom due to nonlinearity of the material. Previous studies have shown that PVA exhibits nonlinear elastic behavior (Chatelin et al., 2014).

4.4. Acoustic properties

Speed-of-sound measured in the phantoms was higher than that measured in biological tissues like healthy skeletal muscle (~1640 vs. 1590 m/s Marsh, 2016), and acoustic attenuation was also higher (~0.7 vs. 0.5 dB/cm/MHz Berger, 1987). Embedding the lattices in homogeneous PVA did not significantly change the speed-of-sound for both phantom samples and had only a minor impact on acoustic attenuation (slightly increasing trend) as compared to PVA alone (Table 3). This indicates that future efforts to tune acoustic properties of the phantoms should involve changing the recipe of the background material rather than the lattice material. For PVA, we will investigate tuning ethylene glycol concentration to control speed-of-sound (Bisht et al., 2024). We also noted that speckle SNR decreased significantly between homogeneous PVA samples and their corresponding composite phantoms, which is to be expected given the presence of the more echogenic lattice structure (Tuthill et al., 1988). Finally, in homogeneous 4% PVA, we observed settling of the acoustic scatterers leading to a gradient in the speckle brightness. We posit that the high acoustic attenuation value measured in these samples can be attributed to this settling.

4.5. Implications for future phantom fabrication

This work presents a proof-of-concept SWEI characterization of anisotropic lattice phantoms that were originally designed for MRE applications. To date, there are few anisotropic phantoms that both mimic the material properties of biological tissue and are constructed using standard and accessible 3D printing techniques. The tunability of the lattice material properties has been demonstrated by modulating printing parameters such as strut diameter, unit cell size, and scaling factor to achieve varying stiffnesses and degrees of anisotropy (Yoon et al., 2024). Independently modulating the stiffness of the underlying “fiber structure” and background matrix of a composite anisotropic phantom enables greater variety of tissue-mimicking phantoms and could also simulate the progression of certain muscle pathologies, such as fatty infiltration or fibrosis (Lovering et al., 2013; Veeger et al., 2021). Additionally, these lattices, made from a PEGDA crosslinking

monomer, have been shown to be robust up to at least 7 months in storage (Yoon et al., 2023). Finally, these phantoms are compatible for multiple elastography modalities (MRE, SWEI) and can be used to facilitate cross-validation between multiple characterization techniques (Eckstein et al., 2024).

4.6. Limitations

It is noted that the lattices were printed from the same design file and were therefore intended to be replicates. However, lattice #1 exhibited higher shear wave speeds and a lower shear anisotropy than lattice #2 when measured in water using 3D-RSWEI. Differences in lattice stiffness could be caused by printing defects or variability in the temperature, resin oxygen level or other variables during printing. Additionally, in fabricating the 4% PVA phantom, we observed a considerable amount of cellulose particle settling prior to the freeze-thaw process. Though the scatterer settling did not impact the stiffness of the PVA or shear wave SNR, the resulting sample exhibited an inhomogeneous acoustic speckle pattern (Fig. 4). Future optimization of composite multimodal phantoms will investigate minimal scatterer settling while attaining material properties comparable to those of biological tissue.

5. Conclusions

In this work, we have characterized anisotropic lattice composite phantoms created for magnetic resonance elastography using 3D-RSWEI and direct mechanical testing. Anisotropic properties were introduced by embedding 3D-printed scaled vintile hydrogel lattice structures in isotropic PVA. Shear wave speeds in all rotational directions and shear anisotropy decreased when the lattices were embedded in PVA. In these composite phantoms, wave dispersion was greater parallel vs. perpendicular to the lattice scaling direction. Speed-of-sound and acoustic attenuation of the composite phantoms were not significantly different from homogeneous PVA. SWEI and DST measurements agreed within 8.4% and 24.1%, respectively, for shear moduli parallel and perpendicular to the scaling direction. These results demonstrate the feasibility of 3D-RSWEI characterization of a non-biological and potentially easily tunable anisotropic phantom for elastography techniques. Future efforts will focus on phantom designs for enhanced repeatability and durability and characterization by both MRE and 3D-RSWEI.

CRediT authorship contribution statement

Shruthi Srinivasan: Conceptualization, Formal analysis, Investigation, Methodology, Software, Visualization, Writing – original draft. **Kevin N. Eckstein:** Conceptualization, Data curation, Investigation, Methodology, Writing – review & editing. **Daniel Yoon:** Conceptualization, Investigation, Methodology, Software. **Ned C. Rouze:** Conceptualization, Formal analysis, Investigation, Methodology, Writing – review & editing. **Kaden D. Bock:** Conceptualization, Data curation, Methodology, Software, Writing – review & editing. **Estela Villacis:** Data curation, Investigation, Methodology, Software. **Philip V. Bayly:** Conceptualization, Funding acquisition, Methodology, Project administration, Supervision, Writing – review & editing. **Kathryn R. Nightingale:** Conceptualization, Funding acquisition, Methodology, Project administration, Supervision, Writing – review & editing.

Declaration of competing interest

The authors declare that they have no known competing financial interests or personal relationships that could have appeared to influence the work reported in this paper.

Acknowledgments

The authors acknowledge our funding sources NIH grant R01EB03 3064.

Data availability

Data will be made available on request.

References

- Alleyne, D., Cawley, P., 1991. A two-dimensional Fourier transform method for the measurement of propagating multimode signals. *J. Acoust. Soc. Am.* 89 (3), 1159–1168.
- American Institute of Ultrasound in Medicine, 2014. Methods for Specifying Acoustic Properties of Tissue Mimicking Phantoms and Objects, second ed. American Institute of Ultrasound in Medicine, Laurel, Md..
- Arao, Y., Fujiura, T., Itani, S., Tanaka, T., 2015. Strength improvement in injection-molded jute-fiber-reinforced polylactide green-composites. *Compos. Part B: Eng.* 68, 200–206.
- Aristizabal, S., Amador, C., Qiang, B., Kinnick, R.R., Nenadic, I.Z., Greenleaf, J.F., Urban, M.W., 2014. Shear wave vibrometry evaluation in transverse isotropic tissue mimicking phantoms and skeletal muscle. *Phys. Med. Biol.* 59 (24), 7735–7752.
- Berger, G., 1987. Optimal precision in ultrasound attenuation estimation and application to the detection of duchenne muscular dystrophy carriers. *Ultrason. Imaging* 9 (1), 1–17.
- Bisht, S.R., Marri, B.P., Karmakar, J., Mercado Shekhar, K.P., 2024. Viscoelastic characterization of phantoms for ultrasound elastography created using low- and high-viscosity poly(vinyl alcohol) with ethylene glycol as the cryoprotectant. *ACS Omega* acsomega.3c09224.
- Caenen, A., Knight, A.E., Rouze, N.C., Bottenus, N.B., Segers, P., Nightingale, K.R., 2020. Analysis of multiple shear wave modes in a nonlinear soft solid: Experiments and finite element simulations with a tilted acoustic radiation force. *J. Mech. Behav. Biomed. Mater.* 107, 103754.
- Chatelin, S., Bernal, M., Deffieux, T., Papadacci, C., Flaud, P., Nahas, A., Boccarda, C., Gennisson, J.-L., Tanter, M., Pernot, M., 2014. Anisotropic polyvinyl alcohol hydrogel phantom for shear wave elastography in fibrous biological soft tissue: A multimodality characterization. *Phys. Med. Biol.* 59 (22), 6923–6940.
- Chen, Q., Ringleb, S.I., Hulshizer, T., An, K.-N., 2005. Identification of the testing parameters in high frequency dynamic shear measurement on agarose gels. *J. Biomech.* 38 (4), 959–963.
- Dong, J., Lee, W.-N., 2022. A numerical-model-based optimization strategy for design and fabrication of transversely isotropic tissue-mimicking phantoms. In: 2022 IEEE International Ultrasonics Symposium. IUS, IEEE, Venice, Italy, pp. 1–3.
- Dorado Cortez, C., Hermite, L., Ramain, A., Mesmann, C., Lefort, T., Pialat, J., 2016. Ultrasound shear wave velocity in skeletal muscle: A reproducibility study. *Diagn. Interv. Imaging* 97 (1), 71–79.
- Dutt, V., Greenleaf, J.F., 1995. Speckle analysis using signal to noise ratios based on fractional order moments. *Ultrason. Imaging* 17 (4), 251–268.
- Dwyer, K.D., Coulombe, K.L., 2021. Cardiac mechanostructure: Using mechanics and anisotropy as inspiration for developing epicardial therapies in treating myocardial infarction. *Bioact. Mater.* 6 (7), 2198–2220.
- Eckstein, K.N., Yoon, D., Ruding, M., Balouchzadeh, R., Thompson-Mazzeo, A., Okamoto, R.J., Johnson, C.L., McGarry, M.D.J., Bayly, P.V., 2024. Mechanically anisotropic phantoms for magnetic resonance elastography. *Magn. Reson. Med. mrm.30394.*
- Emig, R., Zgierski-Johnston, C.M., Timmermann, V., Taberner, A.J., Nash, M.P., Kohl, P., Peyronnet, R., 2021. Passive myocardial mechanical properties: Meaning, measurement, models. *Biophys. Rev.* 13 (5), 587–610.
- Feng, Y., Okamoto, R.J., Namani, R., Genin, G.M., Bayly, P.V., 2013. Measurements of mechanical anisotropy in brain tissue and implications for transversely isotropic material models of white matter. *J. Mech. Behav. Biomed. Mater.* 23, 117–132.
- Fiorentini, S., Sauvage, J., Mostefaoui, S., Lovstakken, L., Salles, S., 2023. Detection of natural pulse waves (PWs) for anisotropy characterization: An in vitro Study. In: 2023 IEEE International Ultrasonics Symposium. IUS, IEEE, Montreal, QC, Canada, pp. 1–4.
- Fromageau, J., Brusseau, E., Vray, D., Gimenez, G., Delachartre, P., 2003. Characterization of PVA cryogel for intravascular ultrasound elasticity imaging. *IEEE Trans. Ultrason. Ferroelectr. Freq. Control* 50 (10), 1318–1324.
- Gennisson, J.-L., Deffieux, T., Macé, E., Montaldo, G., Fink, M., Tanter, M., 2010. Viscoelastic and anisotropic mechanical properties of in vivo muscle tissue assessed by supersonic shear imaging. *Ultrasound Med. Biol.* 36 (5), 789–801.
- Guidetti, M., Lorgna, G., Hammersly, M., Lewis, P., Klatt, D., Vena, P., Shah, R., Royston, T.J., 2019. Anisotropic composite material phantom to improve skeletal muscle characterization using magnetic resonance elastography. *J. Mech. Behav. Biomed. Mater.* 89, 199–208.

- Kasai, C., Namekawa, K., Koyano, A., Omoto, R., 1985. Real-time two-dimensional blood flow imaging using an autocorrelation technique. *IEEE Trans. Sonics Ultrason.* 32 (3), 458–464.
- Knight, A.E., Trutna, C.A., Rouze, N.C., Hobson-Webb, L.D., Caenen, A., Jin, F.Q., Palmeri, M.L., Nightingale, K.R., 2022. Full characterization of *in Vivo* muscle as an elastic, incompressible, transversely isotropic material using ultrasonic rotational 3D shear wave elasticity imaging. *IEEE Trans. Med. Imaging* 41 (1), 133–144.
- Kumar, K., Andrews, M.E., Jayashankar, V., Mishra, A.K., Suresh, S., 2010. Measurement of viscoelastic properties of polyacrylamide-based tissue-mimicking phantoms for ultrasound elastography applications. *IEEE Trans. Instrum. Meas.* 59 (5), 1224–1232.
- Lovering, R.M., Shah, S.B., Pratt, S.J., Gong, W., Chen, Y., 2013. Architecture of healthy and dystrophic muscles detected by optical coherence tomography. *Muscle Nerve* 47 (4), 588–590.
- Marsh, R.L., 2016. Speed of sound in muscle for use in sonomicrometry. *J. Biomech.* 49 (16), 4138–4141.
- Morrow, D.A., Haut Donahue, T.L., Odegard, G.M., Kaufman, K.R., 2010. Transversely isotropic tensile material properties of skeletal muscle tissue. *J. Mech. Behav. Biomed. Mater.* 3 (1), 124–129.
- Okamoto, R.J., Clayton, E.H., Bayly, P.V., 2011. Viscoelastic properties of soft gels: Comparison of magnetic resonance elastography and dynamic shear testing in the shear wave regime. *Phys. Med. Biol.* 56 (19), 6379–6400.
- Oudry, J., Perichon, N., Chatelin, S., Allemann, P., Soler, L., Willinger, R., Sandrin, L., 2009. Validation of vibration-controlled transient elastography by means of dynamic mechanical analysis: Application to *in vivo* / *in vitro* porcine liver. In: 2009 IEEE International Ultrasonics Symposium. IEEE, Rome, pp. 1435–1438.
- Paley, C.T., Knight, A.E., Jin, F.Q., Moavenzadeh, S.R., Pietrosimone, L.S., Hobson-Webb, L.D., Rouze, N.C., Palmeri, M.L., Nightingale, K.R., 2023. Repeatability of rotational 3-D shear wave elasticity imaging measurements in skeletal muscle. *Ultrasound Med. Biol.* 49 (3), 750–760.
- Paley, C.T., Knight, A.E., Jin, F.Q., Moavenzadeh, S.R., Rouze, N.C., Pietrosimone, L.S., Hobson-Webb, L.D., Palmeri, M.L., Nightingale, K.R., 2024. Rotational 3D shear wave elasticity imaging: Effect of knee flexion on 3D shear wave propagation in *in vivo* vastus lateralis. *J. Mech. Behav. Biomed. Mater.* 150, 106302.
- Paulsen, S.J., Mitcham, T.M., Pan, C.S., Long, J., Grigoryan, B., Sazer, D.W., Harlan, C.J., Janson, K.D., Pagel, M.D., Miller, J.S., Bouchard, R.R., 2021. Projection-based stereolithography for direct 3D printing of heterogeneous ultrasound phantoms. *PLoS One* 16 (12), e0260737.
- Pietsch, R., Wheatley, B.B., Haut Donahue, T.L., Gilbrech, R., Prabhu, R., Liao, J., Williams, L.N., 2014. Anisotropic compressive properties of passive porcine muscle tissue. *J. Biomech. Eng.* 136 (11), 111003.
- Prange, M.T., Margulies, S.S., 2002. Regional, directional, and age-dependent properties of the brain undergoing large deformation. *J. Biomech. Eng.* 124 (2), 244–252.
- Rouze, N.C., Deng, Y., Trutna, C.A., Palmeri, M.L., Nightingale, K.R., 2018. Characterization of viscoelastic materials using group shear wave speeds. *IEEE Trans. Ultrason. Ferroelectr. Freq. Control* 65 (5), 780–794.
- Rouze, N.C., Palmeri, M.L., Nightingale, K.R., 2020. Tractable calculation of the Green's tensor for shear wave propagation in an incompressible, transversely isotropic material. *Phys. Med. Biol.* 65 (1), 015014.
- Rouze, N.C., Wang, M.H., Palmeri, M.L., Nightingale, K.R., 2010. Robust estimation of time-of-flight shear wave speed using a radon sum transformation. *IEEE Trans. Ultrason. Ferroelectr. Freq. Control* 57 (12), 2662–2670.
- Smith, D.R., Caban-Rivera, D.A., McGarry, M.D., Williams, L.T., McIlvain, G., Okamoto, R.J., Van Houten, E.E., Bayly, P.V., Paulsen, K.D., Johnson, C.L., 2022. Anisotropic mechanical properties in the healthy human brain estimated with multi-excitation transversely isotropic MR elastography. *Brain Multiphys.* 3, 100051.
- Surry, K.J.M., Austin, H.J.B., Fenster, A., Peters, T.M., 2004. Poly(vinyl alcohol) cryogel phantoms for use in ultrasound and MR imaging. *Phys. Med. Biol.* 49 (24), 5529–5546.
- Tuthill, T., Sperry, R., Parker, K., 1988. Deviations from Rayleigh statistics in ultrasonic speckle. *Ultrason. Imaging* 10 (2), 81–89.
- Tweten, D.J., Okamoto, R.J., Schmidt, J.L., Garbow, J.R., Bayly, P.V., 2015. Estimation of material parameters from slow and fast shear waves in an incompressible, transversely isotropic material. *J. Biomech.* 48 (15), 4002–4009.
- Urban, M.W., Qiang, B., Song, P., Nenadic, I.Z., Chen, S., Greenleaf, J.F., 2016. Investigation of the effects of myocardial anisotropy for shear wave elastography using impulsive force and harmonic vibration. *Phys. Med. Biol.* 61 (1), 365–382.
- Usumura, M., Kishimoto, R., Ishii, K., Hotta, E., Kershaw, J., Higashi, T., Obata, T., Suga, M., 2021. Longitudinal stability of a multimodal visco-elastic polyacrylamide gel phantom for magnetic resonance and ultrasound shear-wave elastography. *PLoS One* 16 (5), e0250667.
- Veeger, T.T.J., Van Zwet, E.W., Al Mohamad, D., Naarding, K.J., Van De Velde, N.M., Hooijmans, M.T., Webb, A.G., Niks, E.H., De Groot, J.H., Kan, H.E., 2021. Muscle architecture is associated with muscle fat replacement in DUCHENNE and BECKER muscular dystrophies. *Muscle Nerve* 64 (5), 576–584.
- Wang, M., Byram, B., Palmeri, M., Rouze, N., Nightingale, K., 2013. Imaging transverse isotropic properties of muscle by monitoring acoustic radiation force induced shear waves using a 2-D matrix ultrasound array. *IEEE Trans. Med. Imaging* 32 (9), 1671–1684.
- Wang, S., Eckstein, K.N., Guertler, C.A., Johnson, C.L., Okamoto, R.J., McGarry, M.D., Bayly, P.V., 2024. Post-mortem changes of anisotropic mechanical properties in the porcine brain assessed by MR elastography. *Brain Multiphys.* 6, 100091.
- Wei, J.C., Cartmill, I.D., Kendall, M.A., Crichton, M.L., 2022. *In vivo*, *in situ* and *ex vivo* comparison of porcine skin for microprojection array penetration depth, delivery efficiency and elastic modulus assessment. *J. Mech. Behav. Biomed. Mater.* 130, 105187.
- Yoon, D., Eckstein, K.N., Ruding, M., Bayly, P.V., 2024. Structural tuning of anisotropic mechanical properties in 3D-Printed hydrogel lattices. *J. Mech. Behav. Biomed. Mater.* 157, 106625.
- Yoon, D., Ruding, M., Guertler, C.A., Okamoto, R.J., Bayly, P.V., 2023. Design and characterization of 3-D printed hydrogel lattices with anisotropic mechanical properties. *J. Mech. Behav. Biomed. Mater.* 138, 105652.
- Zhou, B., Shao, J., Kisby, C.K., Zhang, X., 2020. Ultrasound vibro-elastography for assessing mechanical properties of porcine reproductive tissues in an *ex vivo* model. *Clin. Biomech.* 78, 105093.